Decoding the mechanism for cytotoxicity in thiolato-bridged triosmium carbonyl clusters: from serum reactivity to cellular impact

Xin Liang, Hélène C Bertrand, Nicolas Delsuc, Bohong Huang, Weng Kee Leong, Alvaro Lopez-Sanchez

Decoding the Mechanism for Cytotoxicity in Thiolato-bridged Triosmium Carbonyl Clusters: From Serum Reactivity to Cellular Impact

Xin Liang,[a] Hélène C. Bertrand,[b] Nicolas Delsuc,[b] Bohong Huang,[a] Weng Kee Leong,[a,] and Alvaro Lopez-Sanchez[b]*

[a] School of Chemistry, Chemical Engineering and Biotechnology, Nanyang Technological University, 637371, Singapore

[b] Laboratoire Chimie Physique et Chimie du Vivant CPCV, Département de chimie, Ecole normale supérieure, PSL University, Sorbonne Université, CNRS, 24 rue Lhomond, 75005 Paris, France

*Corresponding author email: chmlwk@ntu.edu.sg

ABSTRACT: Mechanism of action (MoA) studies on the cytotoxic thiolato-bridged triosmium carbonyl clusters $Os_3(CO)_{10}(\mu\text{-H})(\mu\text{-SR})$ (**2**) indicate that their cytotoxicity is associated with increased reactive oxygen species (ROS) generation, G2/M cell cycle arrest, and subsequent apoptosis. Cellular uptake is a key factor, with an increased reactivity of the cluster with serum leading to reduced available concentrations in the medium thereby diminishing its anti-proliferative effect. Reactivity studies reveal that biomolecular interactions occur predominantly at the triosmium core, with a preference for amine-containing species.

INTRODUCTION

Metal carbonyl clusters have recently emerged as promising candidates for anticancer therapy.[1-18] The triruthenium cluster $Ru_3(CO)_9(PTA)_3$ (PTA = 1,3,5-triaza-7-phosphatricyclo[3.3.1.1]decane) (Figure 1) was the first example of a compound containing direct metal–metal bonds to be investigated for chemotherapeutic applications.[11] Other well-studied examples include the lightly stabilized triosmium cluster $Os_3(CO)_{10}(NCCH_3)_2$ (**1**) and the thiolato-bridged triosmium clusters $Os_3(CO)_{10}(\mu\text{-H})(\mu\text{-SR})$ (**2**) (Figure 1). Cluster **1** is a well-known precursor in triosmium carbonyl cluster chemistry, with two labile CH_3CN ligands that can be readily displaced by other ligands and hence behaves, in that restricted sense, in a similar way to cisplatin. Its ligand exchange follows the preference: -SH > -COOH > $-CONH_2$, with steric factors playing a significant role. It has been shown to inhibit thioredoxin reductase (TrxR), causing G2/M cell cycle arrest and inducing apoptosis.[8, 19]

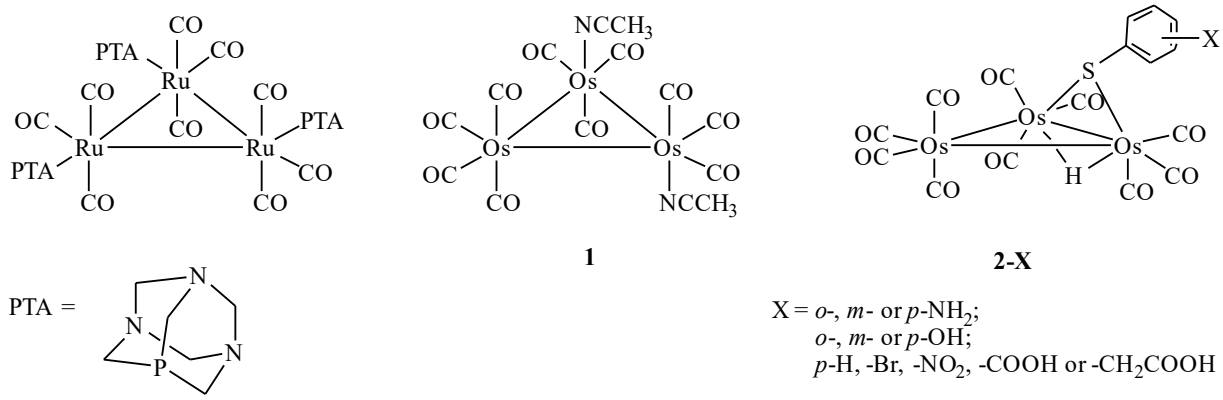

Figure 1. Molecular structures of selected clusters with anticancer potential.

For the clusters **2-X**, it has been shown that, under serum-free conditions, **2-*p*-OH** induced apoptosis via G2/M cell cycle arrest.[3] A structure-activity relationship (SAR) study on **2-X** has shown that their cytotoxicity was affected by interaction with serum, although the underlying mechanism remains to be elucidated.[6] In this study, the mechanism of action (MoA) of **2-X** was further investigated, particularly with respect to the impact of serum.

RESULTS AND DISCUSSION

Apoptosis is essential for maintaining tissue homeostasis by eliminating unhealthy cells without triggering inflammation.[20, 21] Consequently, the induction of apoptosis is a key strategy for the action of many anti-cancer drugs.[22-25] Our previous SAR study demonstrated that the cluster **2-*m*-OH** exhibited good anti-proliferative effects with minimal serum interaction, highlighting its potential as a promising anti-cancer candidate.[6] The induction of apoptosis by **2-*m*-OH** was evident from the morphological changes, including cellular shrinkage and membrane blebbing, which were observed as early as 2 h after treatment, with these features becoming more pronounced over time (Figure S1).[20, 26-28] Nuclear staining after 5 h of treatment revealed smaller, condensed and crescent-shaped nuclei, which is indicative of condensation (pyknosis) and fragmentation (karyorrhexis), with no signs of necrosis (Figure S2).[29-32] Flow cytometric analysis using Annexin V-FITC and propidium iodide (PI) staining,[33, 34] revealed a substantial shift in cell populations, with the proportion of viable cells decreasing from 99.0 ± 0.4% to 54.1 ± 4.1%, while early apoptotic cells increased from 0.71 ± 0.39% to 44.6 ± 3.3% after 24 h treatment, compared to the negative control (Figure 2 and S14).

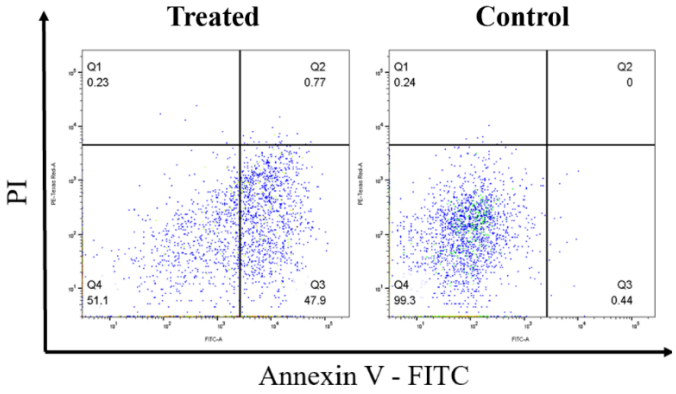

Figure 2. Flow cytometric analysis of MDA-MB-231 cells stained with Annexin V-FITC and propidium iodide (PI). Cells treated with **2-*m*-OH** (5 μM) (left) and control (right) for 24 h in the presence of serum.

The related analogue **2'**, in which the thiolato moiety carries a *2*-quinolyl, was reported to target mitochondria, leading to ROS elevation, caspase activation and subsequent apoptosis.[5] We computed a free energy change ($\Delta G^{\ominus}$) of +87 kJ/mol for a μ-S to κS change in bonding mode, our earlier proposed mechanism of action, illustrated in Scheme 1 for cluster **2'**. Together with its reported IC_{50} of 50–75 μM (in the presence of serum for 24 h),[5] it fitted reasonably well into the same inverse correlation between reactivity and cytotoxicity for clusters **2** (Figures 3 and S13).[6]

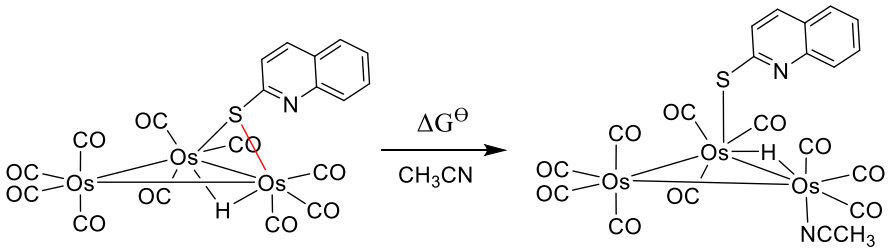

Scheme 1. Proposed mechanism for bonding mode change of cluster **2'** from μ-S to κS, generating a vacant coordination site for a biomolecule (modeled by acetonitrile) used in the $\Delta G^{\ominus}$ computation.

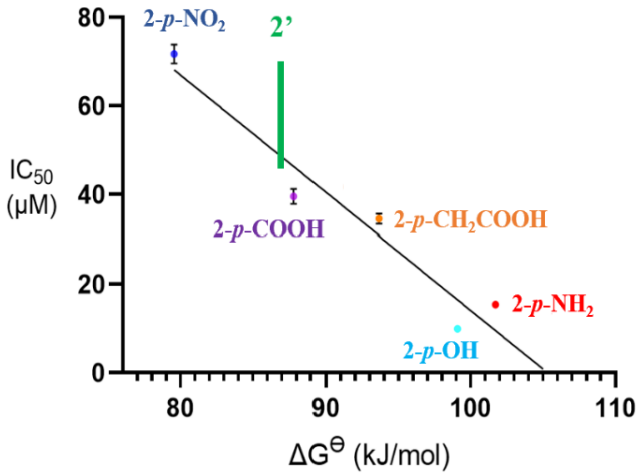

Figure 3. Plot of IC_{50} values (μM, 24 h treatment with serum) versus the calculated $\Delta G^{\ominus}$ (kJ/mol) for selected **2-*p*-X** analogues. The trend line shows a Pearson correlation coefficient of r = –0.97. The green marker highlights the data point for cluster **2′**.

It is thus reasonable to expect that clusters **2** and **2'** share the same mechanistic pathway. Indeed, cells treated with **2-*m*-OH** exhibited a significant increase in reactive oxygen species (ROS) prior to apoptosis.[5] An obvious increase in fluorescence intensity was observed compared to the negative control, as measured using the ROS probe H_2DCFDA (Figures 4 and S3).

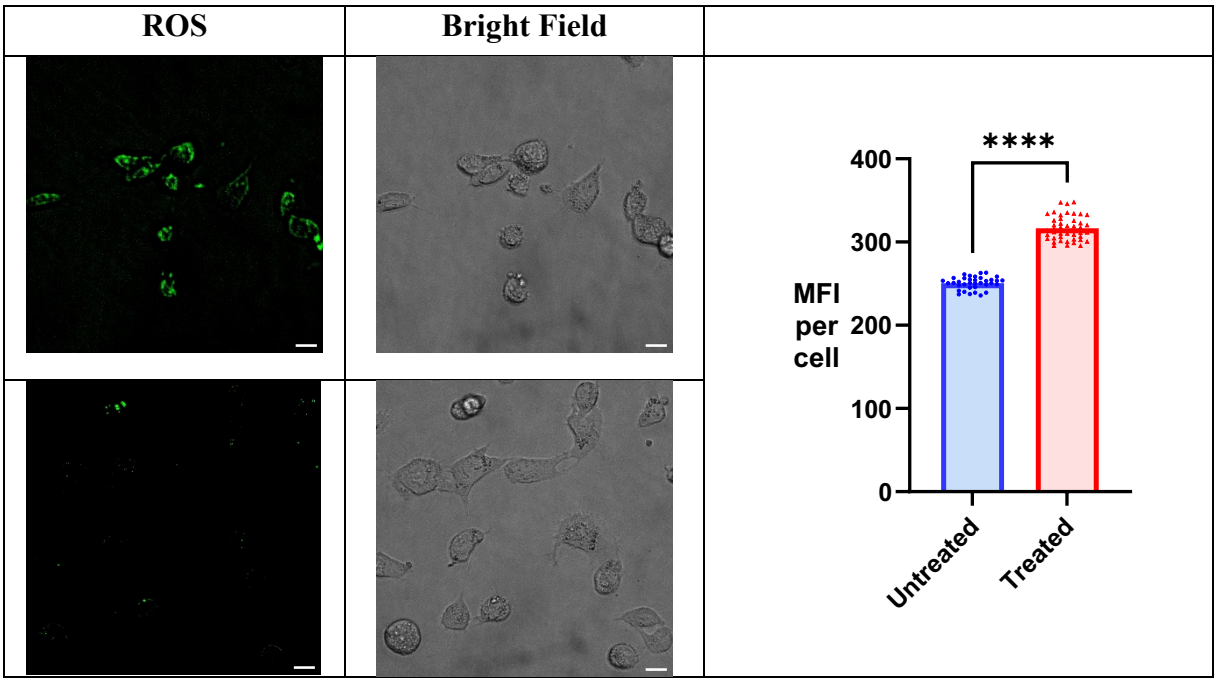

Figure 4. Fluorescence microscopy images showing ROS generation in MDA-MB-231 cells treated with **2-*m*-OH** (5 μM, top) and untreated control (bottom). Cells were incubated for 4 h in the presence of serum. Scale bar: 10 μm. The plot on the right shows the quantification of cellular ROS levels. Data are for mean ± SD from three biological replicates per condition. Statistical significance was determined using Welch's *t* test; ****$p < 0.0001$.

A high level of ROS induces oxidative stress, leading to DNA damage such as strand breaks and base modifications.[35-39] This often results in cell cycle arrest in the G2/M phase, allowing time for DNA repair and if the damage is irreparable, apoptotic pathways are activated to eliminate unhealthy cells.[40,41] Numerous studies have reported that ROS-elevating anticancer agents frequently induce G2/M phase arrest.[42-45] Flow cytometric analysis of propidium iodide (PI)-

stained MDA-MB-231 cells treated with **2-*m*-OH** (5 μM, 24 h) led to an increase in the G2/M population from 18.5 ± 2.1% to 26.8 ± 0.6% and a decrease in the G1 population from 62.1 ± 1.4% to 54.1 ± 0.5% compared to untreated cells (Figure S4). This is thus consistent with **2-*m*-OH** inducing G2/M phase cell cycle arrest through the elevation of ROS.

As mentioned above, our earlier study has shown that there is a strong inverse correlation between reactivity and cytotoxicity for clusters **2** (Figures 3 and S13).[6] It was hypothesized that more reactive clusters are more readily consumed by serum components, thereby reducing their availability for cellular uptake and ultimately diminishing their cytotoxic effects. To test this, the cellular uptake of four **2-*p*-X** clusters (X = OH, NH_2, CH_2COOH, NO_2) was measured as the intracellular osmium levels by ICP-MS. The sample preparation method used for osmium quantification by ICP-MS is critical for the generation of reliable results.[46] The use of oxidative digestion methods (e.g. concentrated nitric acid) is known in the literature to result in the formation of the volatile OsO_4. To minimize such possible biases, we employed a non-oxidative cell lysis using a lysis buffer. Dilution of the lysates with 2% nitric acid was freshly performed right before ICP-MS measurements, keeping the samples at 4 °C until assessment. The results confirmed that intracellular osmium concentrations were significantly reduced in the presence of serum. Notably, a consistent uptake trend was observed under both serum-containing and serum-free conditions: **2-*p*-OH** >> **2-*p*-NH_2** > **2-*p*-CH_2COOH** >> **2-*p*-NO_2** (Figure 5 and Table S1). The low cellular uptake of **2-*p*-NO_2** was also apparent from an attempt at intracellular IR microscopic imaging; MDA-MB-231 breast cancer cells incubated with **2-*p*-NO_2** indicated little or no intracellular cluster compound; hot-spots in the ratio map did not correspond well to cell locations and the spectra appeared to correspond to unreacted **2-*p*-NO_2** (Figures S9 and S12). Clusters with higher cellular uptake generally exhibited greater cytotoxicity under both conditions, suggesting that

cellular uptake plays a key role in determining the cytotoxicity of these clusters (Figure S5). The two clusters **2-*p*-NO₂** and **2-*p*-OH** are noteworthy as they exhibited unusually low and high intracellular uptake and corresponding cytotoxicity, respectively. Although the low cellular uptake of **2-*p*-NO₂** may be related to its lower lipophilicity (log $P_{o/w}$) and higher polarity (MPI),[47-49] its persistently low uptake even after 24 h of incubation in a serum-free environment suggests an additional barrier to intracellular accumulation (Table S1); studies have shown that introducing a nitro group can facilitate recognition by drug efflux pumps, which may explain its poor cellular retention.[50] Once again, an hydroxyl substituent is found to be most promising for enhancing the anti-proliferative effects of these clusters, affording both high cellular uptake and cytotoxicity.

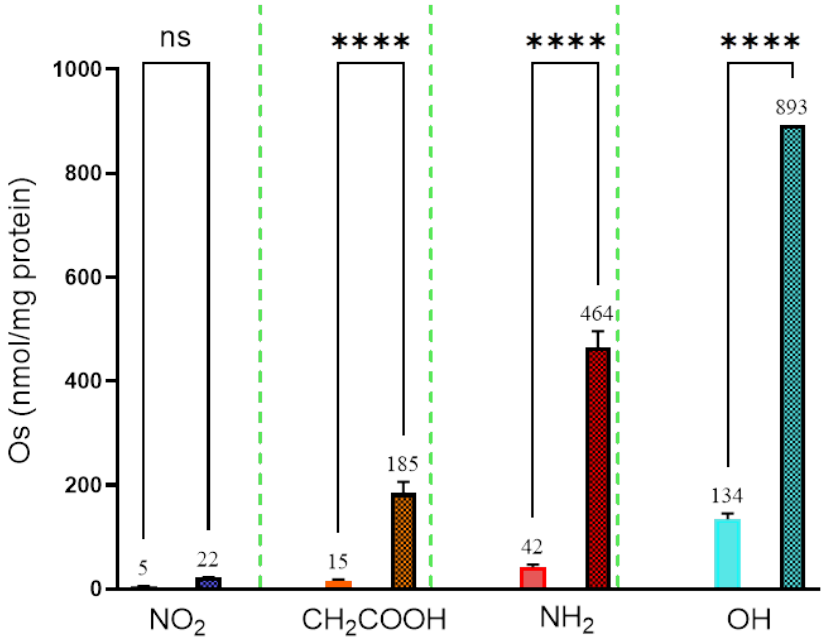

Figure 5. Cellular uptake of triosmium clusters **2-*p*-X**, measured as osmium content (nmol Os/mg protein) in cell lysates by ICP-MS. MDA-MB-231 cells were treated with each cluster (5 μM) for 24 h in the absence (right, latticed bars) or presence (left, solid bars) of serum. Data are presented as mean ± SD. P-values are represented as: ns ($p > 0.05$), * ($p < 0.05$), ** ($p < 0.01$), *** ($p < 0.001$), **** ($p < 0.0001$).

We next attempted to identify possible functional groups on biomolecules that may interact with these clusters by examining the reactivity of the clusters **2-*p*-NH₂** and **2-*p*-NO₂** (the least and most reactive analogues, respectively, based on their $\Delta G^{\ominus}$ values) with some simple organic mimics - imidazole, phenylselenol, *1*-hexanethiol, n-butanoic acid, n-butylamine, and acetamide. In DCM as solvent, there was no observable reaction between **2-*p*-NH₂** and any of these compounds (up to 72 h, as monitored by IR, NMR, and MS). For **2-*p*-NO₂**, spectral changes were observed upon mixing with *1*-hexanethiol and n-butylamine. With *1*-hexanethiol, the ^{1}H NMR spectrum showed a new set of aromatic resonances (distinct from that of free 4-nitrothiophenol) while the metal hydride resonance and CO stretches (IR spectrum) were unchanged (Figure S6). We take this as indicative of interaction at the nitrophenyl ligand rather than ligand dissociation from the triosmium core. With n-butylamine, there was a color change from yellow to red, with a new CO band at 1944 cm^{-1} (IR) and three new metal hydride resonances at –11.9, –11.8, and –15.5 ppm (^{1}H NMR) (Figure S7). These new signals did not match known side products such as $Os_3(\mu\text{-H})(\mu\text{-Cl})(CO)_{10}$ (–14.3 ppm, reaction with trace chloride ions) or $Os_3(\mu\text{-H})(\mu\text{-OH})(CO)_{10}$ (–12.6 ppm, reaction with water), suggesting that the reaction with n-butylamine is at the triosmium core. Similar observations were made in fetal bovine serum (FBS): While **2-*p*-NH₂** showed no reactivity, the IR spectrum for **2-*p*-NO₂** showed immediate change (Figures S7 and S8).

The apparent lack of reactivity of **2-*p*-NH₂** appeared to contradict its observed cytotoxicity. Further investigation revealed that reaction could occur at higher reactant concentration and in a more polar solvent environment. When **2-*p*-NH₂** and cysteine were mixed in d_6-DMSO with a drop of water added, the ^{1}H NMR spectrum showed a new set of aromatic resonances which were shifted upfield relative to those of **2-*p*-NH₂** and distinct from free 4-aminothiophenol; the intensity also increased over time (Figure S10). A DOSY analysis confirmed that these new aromatic signals

originated from a species with a similar diffusion coefficient and hence molecular size as **2-*p*-NH$_2$**; the log of the diffusion coefficients are about -9.52, -9.25 and -9.51 for **2-*p*-NH$_2$**, 4-aminothiophenol and the reaction product, respectively (Figure S11). This is indicative that the reaction product retained the triosmium core structure, with no ligand dissociation.

CONCLUDING REMARKS

In this study, we confirmed that the thiolato-bridged triosmium carbonyl clusters **2** induced apoptosis, accompanied by increased ROS levels and G2/M cell cycle arrest. Their cytotoxic efficacy was governed primarily by cellular accumulation, which was inversely correlated with their reactivity with serum; a more reactive cluster was consumed more readily by serum, leading to reduced intracellular concentration and diminished cytotoxicity. Reactions occurred at the triosmium core, with amine-containing species as likely targets, although the precise nature of this species remained elusive.

EXPERIMENTAL SECTION

All clusters were synthesized following procedures reported in our previous studies.[6] IR spectra were recorded on a Bruker APEX FTIR spectrometer in solution IR cells fitted with KBr windows and a 0.1 mm pathlength, at 2 cm^{-1} resolution. ^{1}H NMR spectra were recorded on a JEOL ECA 500 or Bruker AVIII 400MHz NMR spectrometer. DOSY spectra were acquired on a Bruker Avance III HD 800 MHz NMR spectrometer by Dr. Manfred Wagner at the Max Planck Institute for Polymer Research (MPIP). Chemical shifts are referenced to the residual proton resonance of the solvent. The IR cell imaging experiments were carried out on a Cary 610 infrared microscope equipped with a 128×128 pixels Stingray MCT detector, coupled to a Cary 660 spectrometer equipped with a KBr beam splitter and a Michelson interferometer. Os content in cells was quantified using an Agilent 7850 ICP-MS device.

All test compounds were recrystallized after TLC purification before use in the biological work. Stock solutions of the test compounds were prepared in DMSO and subsequently diluted with specific medium to the working concentrations. The triple-negative breast cancer cells MDA-MB-231, obtained from ATCC, were cultured in Dulbecco′s Modified Eagle′s Medium (Cat# 11995065, Gibco™) supplemented with 10% fetal bovine serum (FBS) and 1% penicillin/streptomycin (P/S) at 37 °C in a 5% CO_2 atmosphere in T25 or T75 culture flasks. Flow cytometry was performed using a BD LSRFortessa™ X-20 flow cytometer. Fluorescent cell images were acquired with a Nikon Ti-E motorized inverted microscope.

Sample preparation for ICP-MS analysis

Cells were seeded in a T25 flask at a density of 1.25×10^6 cells per 5 mL of complete growth medium (1% penicillin/streptomycin and 10% FBS) and incubated for 24 h. The medium was then removed and replaced with the test compound working solution (5 mL, 5 μM in pure DMEM or complete growth medium, prepared from a 5 mM stock in DMSO) and incubated again for 24 h. After treatment, the medium was aspirated, and the cells were washed twice with DPBS (Dulbecco's Phosphate-Buffered Saline). Subsequently, 1 mL of lysis buffer (made by mixing 5700 μL DPBS + 240 μL of a 25X inhibitor cocktail + 60 μL of Triton X-100) was added, and the cells were incubated at room temperature for 5 min. A cell scraper was used to detach the cells from the flask. Cell lysates were collected, sonicated to break up aggregates, and kept at -20 °C. Freshly before ICP-MS measurements, each 800 μL cell lysate was resuspended in 2% aq. nitric acid (1200 μL), filtered through a 0.22 μm filter (CHROMAFIL Xtra PET-20/13, Macherey-Nagel) into a 15 mL conical centrifuge tube, and and kept at 4 °C until ICP-MS assessment on the same day. Normalization was conducted by determining the total protein concentration of cell lysates with a bicinchoninic acid (BCA) assay.

Total protein content determination in cell lysates by BCA assay

BCA (Interchim BC assay Reagent A UP95424A), BSA and $CuSO_4$ (Interchim BC assay Reagent B UP95425A) were purchased from Uptima-Interchim (Montluçon, France). A calibration curve was prepared from a mother solution of 75 µL bovine serum albumin (BSA, InterChim, 2 mg/mL) with 75 µL milliQ water (concentration of 1 mg/mL). A series of eight 1:2 dilutions was performed, including a blank containing only milliQ water.

In a 96-well plate, 25 µL of the calibration solutions were introduced (in duplicates), as well as 3 µL of sonicated cell lysate samples with 22 µL of milliQ water (in triplicates). Aliquots of 200 µL of the revelation solution, consisting of a mixture of 10 mL of BCA and 200 µL of $CuSO_4$ was put into each well. After 30 mins of incubation at 37 °C, absorbance was measured at 560 nm on a Tecan SPARK microplate reader and the calibration scale was used to determine protein concentration in each well (µg/µL). Statistical analyses were performed with the GraphPad Prism 9.5.1 software. The ordinary one-way Anova test was used for comparisons between groups.

IR microscopy analysis

Cells were cultured on IR-transparent calcium fluoride (CaF_2) slides (13 mm diameter × 0.2 mm thickness, IR-grade, double-side polished, tolerance ±0.1 mm) placed in a 12-well plate. Prior to cell seeding, the CaF_2 slides were rinsed with 99% ethanol and allowed to air dry, followed by two washes with Dulbecco's phosphate-buffered saline (DPBS). Cells were then seeded at a density of 1×10^5 cells per well in 1 mL of complete growth medium and incubated at 37 °C with 5% CO_2 for 24 h to allow cell attachment. Following incubation, cells were gently washed once with PBS and treated with 1 mL of the test compound solution (30 µM) in serum-free DMEM (prepared from 5 mM DMSO stock solutions). For time-course analysis, treatments were staggered to yield final incubation times of 2, 3, and 4 h. After treatment, cells were washed twice with DPBS

and fixed with 1 mL of 4% paraformaldehyde (PFA in PBS) for 15 min at room temperature. The fixed cells were then washed twice with PBS and air-dried at room temperature under aluminum foil to prevent light exposure until infrared microscopy analysis.

The images were taken with a 15X magnification 0.62 numerical aperture objective giving a projected pixel size of 5.5×5.5 μm². Spectra were recorded at 8 cm-1 resolution between 800 and 4000 cm-1 with 32 co-added scans at 2.5 Hz mirror speed. The maps obtained were treated on Resolution Pro software (Agilent). A PCA was applied to remove noise and maps were generated at the desired wavenumber or by using a ratio of areas.

Hoechst staining

Cells were plated in 6-well culture plates at a density of 1×10^5 cells per well and incubated at 37 °C in a 5% CO_2 atmosphere for 24 h. After treatment with **2-*m*-OH** for 5 h in the absence of serum, the cells were washed twice with PBS. The cells were then incubated with Hoechst 33342 stain (1 μg/mL in PBS) for 15 mins at room temperature, protected from light. Following staining, the cells were washed three times with PBS to remove excess dye and then visualized using a fluorescence microscope.

ROS staining

Cells were plated in 6-well culture plates at a density of 1×10^5 cells per well and incubated at 37 °C in a 5% CO_2 atmosphere for 24 h. After treatment with **2-*m*-OH** for 4 h in the presence of serum, the cells were washed twice with PBS and then incubated with H_2DCFDA (10 μM in PBS) for 30 min at 37 °C, protected from light. Following the incubation, the cells were washed twice with PBS and then visualized under a fluorescence microscope. For each cell, regions of interest (ROIs) were first defined on the bright-field image and then applied to the corresponding fluorescence channel to measure mean fluorescence intensity (MFI) using ImageJ.

Annexin V-FITC and PI staining

Cells were plated in 6-well culture plates at a density of 1×10^5 cells per well and incubated at 37 °C in a 5% CO_2 atmosphere for 24 h. The cells were then treated with 5 μM **2-*m*-OH** for 24 h in the presence of serum. After treatment, the cells were collected by trypsinization and washed twice with cold PBS to remove any residual media, and resuspended in 1 × binding buffer at a concentration of 1×10^6 cells per ml. Annexin V-FITC (5 μL) was added to the cell suspension and incubated for 15 mins at room temperature in the dark, followed by PI (5 μL) and incubation for an additional 15 mins at room temperature, protected from light. The cells were then analyzed using a flow cytometer.

Reactivity studies

To a solution of the cluster **2-*p*-NO_2** or **2-*p*-NH_2** (10 mg, 0.0644 mmol) in DCM (5 mL), a 3:1 molar ratio of the model compounds (relative to the cluster) was added. The reaction mixture was stirred at 37 °C for 72 h and monitored by IR and ^{1}H NMR spectroscopy. For the reaction with FBS, a solution of the cluster (10 mg, 0.0644 mmol) in DMSO (2 mL) was mixed with FBS (5 mL), stirred at 37 °C and monitored over 72 h by ATR-IR.

Computation studies

Computational studies were performed using density functional theory (DFT) following methods reported in our previous study.[6] Geometry optimizations were carried out by density functional theory (DFT) utilizing Truhlar's M06 hybrid functional.[51] The def2-tzvp basis set was employed for all atoms.[52, 53] Spin-restricted calculations were used for geometry optimization, and harmonic frequencies were then calculated to characterize the stationary points as equilibrium structures with all real frequencies, and to evaluate zero-point energy (ZPE) corrections. Free energies were corrected for vibrational entropy using Grimme's method at a frequency cut-off of

50 cm^{-1},[54] with the program Goodvibes.[55] All calculations were performed using the Gaussian 16 suite of programs.[56]

ASSOCIATED CONTENT

Supporting Information

Additional tables and figures on cytotoxicity, cellular uptake and reactivity, and computational data. These are available free of charge at.

Author Contributions

Xin Liang – all experimental work and design, data analysis, preparation of draft manuscript through to final draft.

Helene C. Bertrand – managed and supervised the research group and laboratory facilities where the ICP-MS and IR microscopy work were conducted and interpretation of the results, assisted in writing of final draft.

Nicolas Delsuc – measurement and interpretation of IR imaging.

Bohong Huang – assisted with the reactivity studies.

Alvaro Lopez-Sanchez – assisted with and interpretation of the ICP-MS results.

Weng Kee Leong – conceptualization, interpretation, writing of final draft.

All authors have given approval to the final version of the manuscript.

Funding Sources

This work was supported by Nanyang Technological University and the Ministry of Education, Singapore through research grants RG12/20 and RG1/21.

Notes

The authors declare no competing financial interest.

ACKNOWLEDGMENTS

Some of the cell studies were conducted in the laboratories of Professor Balazs Zoltan Gulyas at the Lee Kong Chian School of Medicine, Nanyang Technological University; we thank him for their use.

DECLARATIONS

Competing interest

The authors declare no competing interests.

Consent to publish

All authors have given permission to publish.

Ethics declaration

Not applicable.

REFERENCE

(1) Arrais, A.; Gabano, E.; Ravera, M.; Osella, D. Transition Metal Carbonyl Clusters in Biology: A Futile or Niche Research Area? *Inorg. Chim. Acta* **2018**, *470*, 3–10.

(2) Pöthig, A.; Casini, A. Recent Developments of Supramolecular Metal-Based Structures for Applications in Cancer Therapy and Imaging. *Theranostics* **2019**, *9* (11), 3150.

(3) Kong, J. W.; Lam, Z.; Chan, K. H.; Ganguly, R.; Lee, J.-Y. J.; Loo, L.-H.; Webster, R. D.; Wong, Z. X.; Leong, W. K. Group VIII Metal Carbonyl Cluster–Boronic Acid Conjugates: Cytotoxicity and Mode of Action Studies. *ACS Omega* **2021**, *6* (43), 29045–29053.

(4) Lee, H. Z.; Leong, W. K.; Top, S.; Vessières, A. Cytotoxic Triosmium Carbonyl Clusters: A Structure–Activity Relationship Study. *ChemMedChem* **2014**, *9* (7), 1453–1457.

(5) Maillet, A.; Yadav, S.; Loo, Y.; Sachaphibulkij, K.; Pervaiz, S. A Novel Osmium-Based Compound Targets the Mitochondria and Triggers ROS-Dependent Apoptosis in Colon Carcinoma. *Cell Death Dis.* **2013**, *4* (6), e653.

(6) Liang, X.; Leong, W. K. SAR Study on Thiolato-Bridged Triosmium Carbonyl Clusters: Higher Reactivity Does Not Equal Higher Antiproliferative Activity. *J. Med. Chem.* **2024**, *67* (23), 20980–20985.

(7) Kong, K. V.; Liao, L.-D.; Lam, Z.; Thakor, N. V.; Leong, W. K.; Olivo, M. Organometallic Carbonyl Clusters: A New Class of Contrast Agents for Photoacoustic Cerebral Vascular Imaging. *Chem. Commun.* **2014**, *50* (20), 2601–2603.

(8) Koh, W. X.; Coppo, L.; Holmgren, A.; Kong, J. W.; Leong, W. K. Inhibition of Thioredoxin Reductase by Triosmium Carbonyl Clusters. *Chem. Res. Toxicol.* **2020**, *33* (9), 2441–2445.

(9) Nazarov, A. A.; Baquié, M.; Nowak-Sliwinska, P.; Zava, O.; van Beijnum, J. R.; Groessl, M.; Chisholm, D. M.; Ahmadi, Z.; McIndoe, J. S.; Griffioen, A. W. Synthesis and

Characterization of a New Class of Anti-Angiogenic Agents Based on Ruthenium Clusters. *Sci. Rep.* **2013**, *3* (1), 1485.

(10) Colangelo, D.; Ghiglia, A.; Ghezzi, A.; Ravera, M.; Rosenberg, E.; Spada, F.; Osella, D. Water-Soluble Benzoheterocycle Triosmium Clusters as Potential Inhibitors of Telomerase Enzyme. *J. Inorg. Biochem.* **2005**, *99* (2), 505–512.

(11) Allardyce, C. S.; Dyson, P. J. The Interactions of Low Oxidation State Transition Metal Clusters with DNA: Potential Applications in Cancer Therapy. *J. Cluster Sci.* **2001**, *12*, 563–569.

(12) Scalcon, V.; Top, S.; Lee, H. Z. S.; Citta, A.; Folda, A.; Bindoli, A.; Leong, W. K.; Salmain, M.; Vessières, A.; Jaouen, G. Osmocenyl-Tamoxifen Derivatives Target the Thioredoxin System Leading to a Redox Imbalance in Jurkat Cells. *J. Inorg. Biochem.* **2016**, *160*, 296–304.

(13) Reddy, V.; Dayal, D.; Cosenza, S. C.; Reddy, M. R.; Pearl, W. C.; Adams, R. D. Glycal–Ruthenium Carbonyl Clusters: Syntheses, Characterization, and Anticancer Activity. *J. Organomet. Chem.* **2009**, *694* (6), 959–967.

(14) Nazarov, A.; Nosova, Y. N.; Mikhalev, O.; Kovaleva, O.; Dyson, P.; Milaeva, E. Antiproliferative Activity of Ruthenium and Osmium Clusters with Phosphine Ligands. *Russ. Chem. Bull.* **2016**, *65*, 546–549.

(15) Peña, B.; Barhoumi, R.; Burghardt, R. C.; Turro, C.; Dunbar, K. R. Confocal Fluorescence Microscopy Studies of a Fluorophore-Labeled Dirhodium Compound: Visualizing Metal–Metal Bonded Molecules in Lung Cancer (A549) Cells. *J. Am. Chem. Soc.* **2014**, *136* (22), 7861–7864.

(16) Kong, K. V.; Leong, W. K.; Lim, L. H. K. Induction of Apoptosis by Hexaosmium Carbonyl Clusters. *J. Organomet. Chem.* **2009**, *694* (6), 834–839.

(17) Lee, H. Z. S.; Leong, W. K.; Top, S.; Vessières, A. Cytotoxic Triosmium Carbonyl Clusters: A Structure–Activity Relationship Study. *ChemMedChem* **2014**, *9* (7), 1453–1457.

(18) Kong, K. V.; Leong, W. K.; Ng, S. P.; Nguyen, T. H.; Lim, L. H. Osmium Carbonyl Clusters: A New Class of Apoptosis Inducing Agents. *ChemMedChem* **2008**, *3* (8), 1269–1275.

(19) Lee, J. J. Y.; Leong, W. K. Towards Understanding the Mode of Action of the Cytotoxic Triosmium Carbonyl Cluster $Os_3(CO)_{10}(NCCH_3)_2$: Its Reactivity with Amino Acids and Oligopeptides. *J. Organomet. Chem.* **2020**, *924*, 121459.

(20) Elmore, S. Apoptosis: A Review of Programmed Cell Death. *Toxicol. Pathol.* **2007**, *35* (4), 495–516.

(21) Gavrilescu, L. C.; Denkers, E. Y. Apoptosis and the Balance of Homeostatic and Pathologic Responses to Protozoan Infection. *Infect. Immun.* **2003**, *71* (11), 6109–6115.

(22) Sharma, A.; Boise, L. H.; Shanmugam, M. Cancer Metabolism and the Evasion of Apoptotic Cell Death. *Cancers (Basel)* **2019**, *11* (8).

(23) Carneiro, B. A.; El-Deiry, W. S. Targeting Apoptosis in Cancer Therapy. *Nat. Rev. Clin. Oncol.* **2020**, *17* (7), 395–417.

(24) Chaudhry, G.-e.-S.; Md Akim, A.; Sung, Y. Y.; Sifzizul, T. M. T. Cancer and Apoptosis: The Apoptotic Activity of Plant and Marine Natural Products and Their Potential as Targeted Cancer Therapeutics. *Front. Pharmacol.* **2022**, *13*, Review.

(25) Pistritto, G.; Trisciuoglio, D.; Ceci, C.; Garufi, A.; D'Orazi, G. Apoptosis as Anticancer Mechanism: Function and Dysfunction of Its Modulators and Targeted Therapeutic Strategies. *Aging (Albany NY)* **2016**, *8* (4), 603–619.

(26) Saraste, A.; Pulkki, K. Morphologic and Biochemical Hallmarks of Apoptosis. *Cardiovasc. Res.* **2000**, *45* (3), 528–537.

(27) Kari, S.; Subramanian, K.; Altomonte, I. A.; Murugesan, A.; Yli-Harja, O.; Kandhavelu, M. Programmed Cell Death Detection Methods: A Systematic Review and a Categorical Comparison. *Apoptosis* **2022**, *27* (7), 482–508.

(28) Park, W.; Wei, S.; Kim, B.-S.; Kim, B.; Bae, S.-J.; Chae, Y. C.; Ryu, D.; Ha, K.-T. Diversity and Complexity of Cell Death: A Historical Review. *Exp. Mol. Med.* **2023**, *55* (8), 1573–1594.

(29) Hou, L.; Liu, K.; Li, Y.; Ma, S.; Ji, X.; Liu, L. Necrotic Pyknosis Is a Morphologically and Biochemically Distinct Event from Apoptotic Pyknosis. *J. Cell Sci.* **2016**, *129* (16), 3084–3090.

(30) Fujikawa, D.; Shinmei, S.; Cai, B. Kainic Acid-Induced Seizures Produce Necrotic, Not Apoptotic, Neurons with Internucleosomal DNA Cleavage: Implications for Programmed Cell Death Mechanisms. *Neuroscience* **2000**, *98* (1), 41–53.

(31) Burgoyne, L. A. The Mechanisms of Pyknosis: Hypercondensation and Death. *Exp. Cell Res.* **1999**, *248* (1), 214–222.

(32) Galvão, I.; Athayde, R. M.; Perez, D. A.; Reis, A. C.; Rezende, L.; de Oliveira, V. L. S.; Rezende, B. M.; Gonçalves, W. A.; Sousa, L. P.; Teixeira, M. M.; et al. ROCK Inhibition Drives Resolution of Acute Inflammation by Enhancing Neutrophil Apoptosis. *Cells* **2019**, *8* (9).

(33) Calianese, D. C.; Birge, R. B. Biology of Phosphatidylserine (PS): Basic Physiology and Implications in Immunology, Infectious Disease, and Cancer. *Cell Commun. Signal.* **2020**, *18* (1), 41.

(34) Audo, R.; Hua, C.; Hahne, M.; Combe, B.; Morel, J.; Daien, C. I. Phosphatidylserine Outer Layer Translocation Is Implicated in IL-10 Secretion by Human Regulatory B Cells. *PLoS One* **2017**, *12* (1), e0169755.

(35) Yu, T.-W.; Anderson, D. Reactive Oxygen Species-Induced DNA Damage and Its Modification: A Chemical Investigation. *Mutat. Res., Fundam. Mol. Mech. Mutagen.* **1997**, *379* (2), 201–210.

(36) Cadet, J.; Wagner, J. R. DNA Base Damage by Reactive Oxygen Species, Oxidizing Agents, and UV Radiation. *Cold Spring Harb. Perspect. Biol.* **2013**, *5* (2), a012559.

(37) Cadet, J.; Davies, K. J. A. Oxidative DNA Damage & Repair: An Introduction. *Free Radic. Biol. Med.* **2017**, *107*, 2–12.

(38) Yu, Y.; Cui, Y.; Niedernhofer, L. J.; Wang, Y. Occurrence, Biological Consequences, and Human Health Relevance of Oxidative Stress-Induced DNA Damage. *Chem. Res. Toxicol.* **2016**, *29* (12), 2008–2039.

(39) Barzilai, A.; Yamamoto, K.-I. DNA Damage Responses to Oxidative Stress. *DNA Repair* **2004**, *3* (8–9), 1109–1115.

(40) Srinivas, U. S.; Tan, B. W. Q.; Vellayappan, B. A.; Jeyasekharan, A. D. ROS and the DNA Damage Response in Cancer. *Redox Biol.* **2019**, *25*, 101084.

(41) Maynard, S.; Schurman, S. H.; Harboe, C.; de Souza-Pinto, N. C.; Bohr, V. A. Base Excision Repair of Oxidative DNA Damage and Association with Cancer and Aging. *Carcinogenesis* **2009**, *30* (1), 2–11.

(42) Moon, D.-O.; Kim, M.-O.; Choi, Y. H.; Hyun, J. W.; Chang, W. Y.; Kim, G.-Y. Butein Induces G2/M Phase Arrest and Apoptosis in Human Hepatoma Cancer Cells through ROS Generation. *Cancer Lett.* **2010**, *288* (2), 204–213.

(43) Zhang, Z.; Leonard, S. S.; Huang, C.; Vallyathan, V.; Castranova, V.; Shi, X. Role of Reactive Oxygen Species and MAPKs in Vanadate-Induced G2/M Phase Arrest. *Free Radic. Biol. Med.* **2003**, *34* (10), 1333–1343.

(44) Wang, H.; Zhang, T.; Sun, W.; Wang, Z.; Zuo, D.; Zhou, Z.; Li, S.; Xu, J.; Yin, F.; Hua, Y. Erianin Induces G2/M-Phase Arrest, Apoptosis, and Autophagy via the ROS/JNK Signaling Pathway in Human Osteosarcoma Cells in Vitro and in Vivo. *Cell Death Dis.* **2016**, *7* (6), e2247.

(45) Hao, X.; Bu, W.; Lv, G.; Xu, L.; Hou, D.; Wang, J.; Liu, X.; Yang, T.; Zhang, X.; Liu, Q. Disrupted Mitochondrial Homeostasis Coupled with Mitotic Arrest Generates Antineoplastic Oxidative Stress. *Oncogene* **2022**, *41* (3), 427–443.

(46) Klose, M. H. M.; Hejl, M.; Heffeter, P.; Jakupec, M. A.; Meier-Menches, S. M.; Berger, W.; Keppler, B. K. Post-Digestion Stabilization of Osmium Enables Quantification by ICP-MS in Cell Culture and Tissue. *Analyst* **2017**, *142*(13), 2327-2332. DOI:10.1039/C7AN00350A.

(47) Winiwarter, S.; Ridderström, M.; Ungell, A.-L.; Andersson, T.; Zamora, I. Use of Molecular Descriptors for Absorption, Distribution, Metabolism, and Excretion Predictions. *Compr. Med. Chem. II* **2006**, *5*, 531–554.

(48) Zhu, Q.; Lu, Y.; He, X.; Liu, T.; Chen, H.; Wang, F.; Zheng, D.; Dong, H.; Ma, J. Entropy and Polarity Control the Partition and Transportation of Drug-like Molecules in Biological Membrane. *Scientific Reports* **2017**, *7* (1), 17749.

(49) Wang, S.; Konig, G.; Roth, H.-J.; Fouché, M.; Rodde, S.; Riniker, S. Effect of flexibility, lipophilicity, and the location of polar residues on the passive membrane permeability of a series of cyclic decapeptides. *J. Med. Chem.* **2021**, *64* (17), 12761-12773.

(50) Bennion, B.J.; Be, N.A.; McNerney, M.W.; Lao, V.; Carlson, E.M.; Valdez, C.A.; Malfatti, M.A.; Enright, H.A.; Nguyen, T.H; Lightstone, F.C.; Carpenter, T.S. Predicting a Drug's Membrane Permeability: A Computational Model Validated With *in Vitro* Permeability Assay Data. *J. Phys. Chem. B* **2017**, *121*(20), 5228–5237.

(51) Zhao, Y.; Truhlar, D. G. The M06 suite of density functionals for main group thermochemistry, thermochemical kinetics, noncovalent interactions, excited states, and transition elements: two new functionals and systematic testing of four M06-class functionals and 12 other functionals. *Theoretical Chemistry Accounts* **2008**, *120* (1), 215-241. DOI: 10.1007/s00214-007-0310-x.

(52) Weigend, F.; Ahlrichs, R. Balanced basis sets of split valence, triple zeta valence and quadruple zeta valence quality for H to Rn: Design and assessment of accuracy. *Physical Chemistry Chemical Physics* **2005**, *7* (18), 3297-3305, 10.1039/B508541A. DOI: 10.1039/B508541A.

(53) Weigend, F. Accurate Coulomb-fitting basis sets for H to Rn. *Physical Chemistry Chemical Physics* **2006**, *8* (9), 1057-1065, 10.1039/B515623H. DOI: 10.1039/B515623H.

(54) Grimme, S. Supramolecular binding thermodynamics by dispersion-corrected density functional theory. *Chemistry* **2012**, *18* (32), 9955-9964. DOI: 10.1002/chem.201200497 From NLM.

(55) Luchini, G.; Alegre-Requena, J.; Funes-Ardoiz, I.; Paton, R. GoodVibes: automated thermochemistry for heterogeneous computational chemistry data [version 1; peer review: 2 approved with reservations]. *F1000Research* **2020**, *9* (291). DOI: 10.12688/f1000research.22758.1.

(56) Frisch, M. J.; Trucks, G. W.; Schlegel, H. B.; Scuseria, G. E.; Robb, M. A.; Cheeseman, J. R.; Scalmani, G.; Barone, V.; Petersson, G. A.; Nakatsuji, H.; et al. Gaussian 16 Rev. C.01. **2016**.